J Nanostruct 16(4): 5900-5912, Autumn 2026

RESEARCH PAPER

Lithium-Doped Copper Oxide Nanoparticles: Defect Development and Augmented Antibacterial Efficacy against Oral Pathogens

*Noor Ameer [1], Noor Raed Hadi [2], Ranya Mahmood Mohammed [2], Faten A. Mahdi [3], Hussein Tami Sim [2]**

[1] *Department of Laser Physics, College of Science for Women, University of Babylon, Hilla, Iraq*

[2] *Department of Physics, College of Science, University of Babylon, Babylon, Iraq*

[3] *Department of Physics, College of Education for Pure Science, University of Babylon, Babylon, Iraq*

ARTICLE INFO

Article History:
Received 05 June 2026
Accepted 24 August 2026
Published 01 October 2026

Keywords:
Antibacterial activity
CuO NPs
Oral Healthcare
Sol-gel method

ABSTRACT

Pure CuO nanoparticles and Li-doped CuO nanoparticles with various concentrations of Li (1% and 5%) were synthesized by the sol-gel method. The synthesized nanoparticles were characterized in detail for structural, elemental, morphological, optical, and antibacterial properties. X-ray diffraction showed only a single monoclinic CuO phase in all samples, with no evidence of secondary phases (the incorporation of Li did not alter the basic crystal structure). The crystals grew further and coalesced into larger domains after doping, as evidenced by the increasing average crystallite size from 28.6 nm for pure CuO to 34.5 nm (1% Li- doping) and 37.0 nm (5% Li- doping). Energy-dispersive X-ray spectroscopy confirmed the presence of Cu and O in the absence of contamination, while direct detection of Li was limited by its low atomic number. Results of morphological analysis indicated a typical quasi-spherical morphology, with increased agglomeration at higher lithium concentrations. The optical measurements revealed a reduction in the band gap from 1.75 eV for pure CuO to 1.48 eV in the 5% Li-doped sample. The decrease was attributed to Li defects, oxygen vacancies, and impurity-related electronic states. All samples have shown the antagonistic activity against *Enterococcus faecalis (E. faecalis) and Prevotella intermedia (P. intermedia)*. The 5% Li-doped CuO NPs samples have shown the highest activity among all the samples. This enhancement is associated with defect-driven charge separation and the generation of reactive oxygen species, leading to oxidative damage in bacterial cells. Finally, the changes in the structural and electronic structures and the defect density were significant. All of these characteristics contributed to improved antibacterial activity applicable to oral healthcare applications.

How to cite this article
Ameer N., Raed Hadi N., Mahmood Mohammed R. et al. Lithium-Doped Copper Oxide Nanoparticles: Defect Development and Augmented Antibacterial Efficacy against Oral Pathogens. J Nanostruct, 2026; 16(4):5900-5912. DOI: 10.22052/JNS.2026.04.117

INTRODUCTION

Oral diseases are among the most serious global health problems that affect an estimated 3.5 to 3.7 billion people in the world [1–4]. Dental caries and periodontal diseases are some of the most common chronic conditions across all age groups [5, 6]. The development of dental caries and gingivitis is closely related to oral pathogens,

* *Corresponding Author Email: sci918.hussein.tami@uobabylon.edu.iq*

This work is licensed under the Creative Commons Attribution 4.0 International License.
To view a copy of this license, visit http://creativecommons.org/licenses/by/4.0/.

including *Streptococcus mutans, Lactobacillus acidophilus, Enterococcus faecalis, Prevotella intermedia, and Porphyromonas gingivalis*, which adhere to oral surfaces and form biofilms on teeth and mucosal surfaces, or cause tissue damage by promoting enamel demineralization [7–10].

Antibacterial mouthwashes and systemic antibiotics are used for treating oral infections. However, repeated use may lead to side effects, damage to the normal oral microbiota, and bacterial resistance [11, 12]. In addition, traditional antimicrobial agents may be less effective against bacterial biofilms. The poor efficacy of most antibiotics in vivo, environmental pollution, and the worldwide emergence of multidrug-resistant bacteria have stimulated the demand for alternative antibacterial materials with high potency and favorable biocompatibility [13–16].

Metal oxide nanoparticles have attracted much attention due to their large surface area, high chemical stability, and high reducibility [17]. Of these, copper oxide nanoparticles stand out among intrinsic semiconductor metal oxide nanoparticles as promising candidates due to their low cost, semiconducting nature, and broad-spectrum antibacterial activity against pathogens [18–20]. Their antimicrobial action is predominantly related to direct contact with the bacterial membranes, Cu^{2+} ion release of the material, and generation of reactive oxygen species that can damage cellular membranes, proteins, enzymes, and genetic material [21–23].

The antibacterial activity of CuO nanoparticles can be enhanced by doping with controlled elements. Lithium is used as a dopant due to its small ionic radius and monovalent charge, and can occupy or distort the CuO lattice, causing minor structural disruption [24, 25]. For example, the

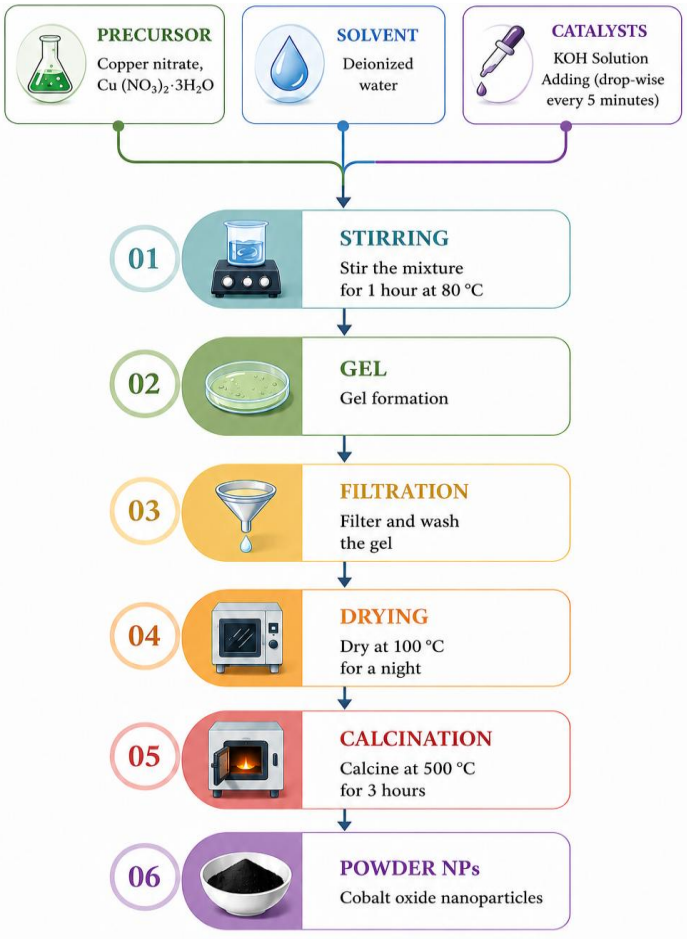


Fig. 1. Flowchart of the powder NPs synthesis process.

CC BY

incorporation of lithium can alter lattice defects, surface charge, particle growth, and electrical behavior, thereby promoting higher surface reactivity and increasing the particle contact with bacterial cells [26–28]. It can even facilitate the release of Cu^{2+} and the generation of ROS, thereby inducing oxidative stress and enhancing antibacterial activity [29, 30].

Several methods for preparing metal oxide nanoparticles include solid-state reaction, coprecipitation, hydrothermal synthesis, combustion, microwave-assisted synthesis, chemical vapor deposition, and the sol-gel technique [31, 32]. Of these, the sol-gel method is widely suitable for preparing doped CuO nanoparticles as it allows the homogeneous mixing of precursors with excellent stoichiometric control and dopant concentration [33–37]; operating at relatively low processing temperatures, in higher purity and better control of particle size and composition. The uniform lithium distribution and reproducible antibacterial properties are attributed to these advantages [38–40].

The antimicrobial activity of CuO nanoparticles has been extensively studied, but their activity against oral pathogenic bacteria has not been well determined under the conditions of lithium doping. Most of these reports have focused on the structural, optical, or antimicrobial properties of CuO-based nanoparticles, with only the general relationship between lithium-induced modulations and antibacterial activity being determined.

The present work aims to investigate the synthesis and antibacterial activity of lithium-doped CuO nanoparticles against pathogenic bacteria commonly found in oral conditions, using the sol-gel method. The objective of the work is to study the effect of Li dopant concentrations on the structure and surface properties of CuO and to relate these changes to the antibacterial properties.

MATERIASL AND METHODS

Synthesis of Pure CuO NPs

Pure CuO NPs were prepared by the sol-gel method. Copper nitrate, Cu $(NO_3)_2 \cdot 3H_2O$, was dissolved in deionized water to prepare a 0.1 mol/L solution. The pH of 800 mL of deionized water was adjusted to 9.75 by adding potassium hydroxide (KOH) solution; however, during the addition, the pH of the combined solution decreased due to salt hydrolysis. The pH was kept at 9.75 by gradually adding KOH solution (drop-wise every 5 minutes). The gel material Cu $(OH)_2$ was formed after placing the solution on the Hotplate Stirrer for 3 hours and stirring at moderate speed at 80°C. The precipitate was cooled to room temperature, filtered, and washed more than five times with deionized water. The solid obtained was oven-dried at 100 °C overnight, then calcined at 500 °C for 3 hours to provide the final product. The synthesis process for CuO NPs is presented in the flowchart in Fig. 1. All the materials and reagents used in this work were bought from commercial suppliers and used

Table 1. Debye- Scherrer parameters for calculating pure CuO NPsand doped CuO crystal size.

Reflection Planes	P. CuO			1 % Li- doped CuO			5 % Li- doped CuO		
	2θ (deg)	FWHM	Crystallite Size (nm)	2θ (deg)	FWHM	Crystallite Size (nm)	2θ (deg)	FWHM	Crystallite Size (nm)
(110)	32.857	0.177	46.8	32.775	0.203	40.8	32.949	0.203	40.8
(-111)	35.875	0.335	24.9	35.727	0.124	67.3	35.919	0.137	61.0
(111)	39.078	0.282	29.9	38.944	0.124	68.0	39.058	0.137	61.5
(20-2)	46.559	0.361	24.0	46.526	0.309	28.0	46.609	0.361	24.0
(-202)	49.125	0.309	28.3	48.990	0.203	43.0	49.105	0.256	34.1
(020)	53.779	0.626	14.2	53.668	0.361	24.7	53.808	0.361	24.7
(202)	58.611	0.309	29.5	58.534	0.414	22.0	58.653	0.282	32.3
(-113)	61.897	0.150	61.8	61.795	0.256	36.2	61.848	0.203	45.6
(022)	66.757	0.256	37.2	66.469	0.282	33.7	66.563	0.229	41.5
(220)	68.375	0.467	20.6	68.321	0.520	18.5	68.473	0.203	47.3
(311)	72.669	0.467	21.1	72.608	0.309	31.9	72.662	0.309	31.9
	The average crystallite size		28.6	The average crystallite size		34.5	The average crystallite size		37.0

CC BY

without further purification.

Synthesis of Li- doped CuO NPs

The sol-gel technique was applied to synthesize Li-doped CuO NPs at different lithium doping concentrations of 1%, and 5% (mol/L) (Li- CuO mole ratio 1:100, and 5:100, and thus, correspondingly, CuO of 99%, and 95%, respectively). For all procedures, the molarity was kept at 0.1 mol/L in 600 mL of deionized water. The solvent involved 14.350 g of copper nitrate hexahydrate $Cu(NO_3)_2{\cdot}3H_2O$ and 0.0414 g of lithium nitrate ($LiNO_3$) in the 1% Li-doped formulation. For the 5% Li-doped formulation, 13.771 g of $Cu(NO_3)_2{\cdot}3H_2O$ and 0.207 g of $LiNO_3$ were used. Each of these solutions was then adjusted to pH 9.75 (the final pH), and the pH was maintained throughout the reaction by the addition of KOH solution dropwise every five minutes, due to the reduction of pH from salt hydrolysis. The solutions were subsequently heated at 80 °C for 4 hours with mild magnetic stirring to produce the gels. The obtained gels were cooled to room temperature, filtered, and thoroughly washed with deionized water to remove residual ions. The precipitates obtained were dried overnight at 100 °C and then calcined at 500 °C for 3 hours to yield the final Li-doped CuO NPs.

Characterization of Pure CuO NPs and doped CuO NPs powder

To characterize our synthesized pure and doped CuO NPs, we performed phase and structural identification using the PanAlytical Aeris Benchtop X-ray Diffractometer 40kW, 7.5 mA with a Cu-Kα radiation source (0.154 nm). Analyzed the data using X'pert HighScore Plus software. Also refined the lattice parameters, profile half-widths (u, v, w), site-occupancy factor, preferred orientation, and peak-shape parameters. A field emission scanning electron microscope (FESEM, Zeiss Supra 35) was used for investigating the morphology of pure and doped CuO NPs. For further analysis of elemental composition and dopant incorporation, energy dispersive X-ray spectroscopy (EDX) was used. The presence of Cu, O and dopant components in the prepared pure and doped CuO NPs was verified by this method. For the optical characterization, UV-visible spectroscopy (UV-vis, Varian Cary Win UV 100) and photoluminescence spectroscopy (PL, Jobin Yvon HR 800 UV) were performed. The characterization results were utilized to identify

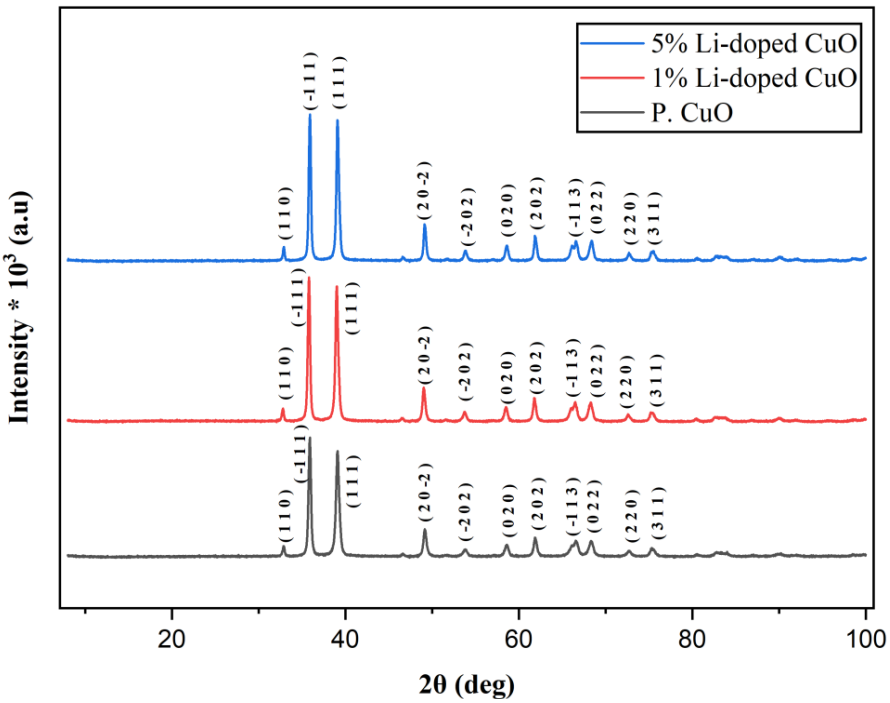


Fig. 2. XRD pattern of the obtained pure and doped CuO NPs.

CC BY

the sample with the best growth properties.

Antibacterial

Antibacterial activity of pure and doped CuO NPs against oral bacterial isolates *E. faecalis* (Gram-positive) and *P. intermedia* (Gram-negative) was determined by the agar well diffusion method. The same procedure was adopted at concentrations of 128, 256, 512, and 1024 µg/mL [15]; only slight modifications were needed.

Each bacterial isolate was grown overnight in nutrient broth at 37 °C (18–24 hours) to obtain log-phase cells. After incubation, serial dilutions of the samples were prepared, and 0.1 mL was plated on nutrient agar plates to allow appropriate growth, with short incubations (24 hours at 37 °C) [23]. Next, one colony isolated from this was placed in a 5-mL sterile normal saline and adjusted according to the turbidity of the SOMS9X standard solution, approximately 1.5×10^8 CFU/mL.

The bacterial suspension was prepared, evenly and gently spread on Mueller-Hinton agar plates with a sterile cotton swab, and allowed to stand for 10 min to allow absorption. Wells approximately 5 mm in diameter were aseptically punched into the agar (five wells per plate). Agar plugs were removed from their respective plates, and 50 µL of purified and crude EPS were added to their respective wells using a micropipette, while distilled water was added to the central well as a negative control. The inoculated plates were incubated at 37 °C for 18 hours, and the antibacterial activity was determined by measuring the diameter of inhibition zones around each well. In this way, the effect of the EPS on Gram-positive and Gram-negative oral pathogens could be comparatively evaluated.

RESULTS AND DISCUSSION

Structural Studies

Fig. 2 shows the XRD patterns for the synthesized pure and doped CuO NPs. The XRD results of pure CuO NPs exhibit the peaks of the diffraction at 32.857°, 35.875°, 39.078°, 46.559°, 49.125°, 53.779°, 58.611°, 61.897°, 66.757°, 68.375° and 72.669° with a slight shift in position for 1% and 5% Li- doped CuO NPs (see Table 1). These peaks are corresponding to the crystallographic planes (110), (-111), (111), (20-2), (-202), (020), (202), (-113), (022), (220), and (311). The absence of additional diffraction peaks supports the formation of a pure monoclinic CuO phase, indicating the absence of secondary lithium related phases [41–43].

This confirms successful incorporation of Li+ ions into the CuO lattice without changing its basic crystal structure. Table 1 shows the changes in peak positions and widths observed as Li concentration increases to 1% and 5%. According to Bragg's law [44, 45], Eq. 1:

$$2d\sin\theta = n\lambda \quad (1)$$

The variation in position of these peak shifts reflects the d-spacing due to lattice distortion which results from substitution of Cu^{2+} by Li^{+} ions. The exchange surface generates local structural stress due to divergence in ionic size and charge, resulting in a minor metamorphosis of lattice parameters. A further gradual widening of diffraction peaks with the increase of Li content indicates a growth in microstructural defects and lattice strain in the crystal [46, 47].

The diffraction peaks of CuO match the standard data from The Joint Committee on Powder Diffraction Standards (JCPDS) [JCPDS

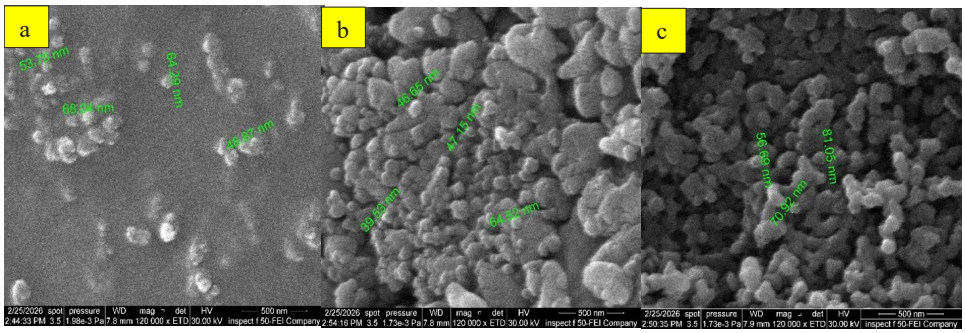


Fig. 3. FESEM images (a) pure CuO, (b) 1% Li-doped CuO, and (c) 5% Li-doped CuO.

file: 45–0946] [48, 49]. Scherrer's formula of Eq 2. A simple Scherrer equation [50, 51] was then used for estimating the average crystallite sizes. The average crystallite sizes of pure CuO NPs are approximately 28.6 nm, and they increased to 34.5 nm and 37.0 nm by doping with Li at concentrations of 1% and 5%, respectively.

An increase in crystallite size with Li can be explained by dopant-induced agglomeration of particles and coalescence of grains during calcination. Li^+ ions increase interparticle couplings and, therefore, facilitate the aggregation of smaller crystallites to larger particle clusters. This is a common behavior in doped oxide systems [52–54]. These systems have been found to use, with increasing amounts of dopants(s), for the crystals to grow together.

Furthermore, in addition to increasing the crystallite size, Li intercalation is expected to create lattice defects (oxygen vacancies) and induce macrostrain in CuO. These defect states play an important role in influencing the physicochemical [55, 56] and antibacterial properties, as well as the electronic properties of materials (Eq. 2).

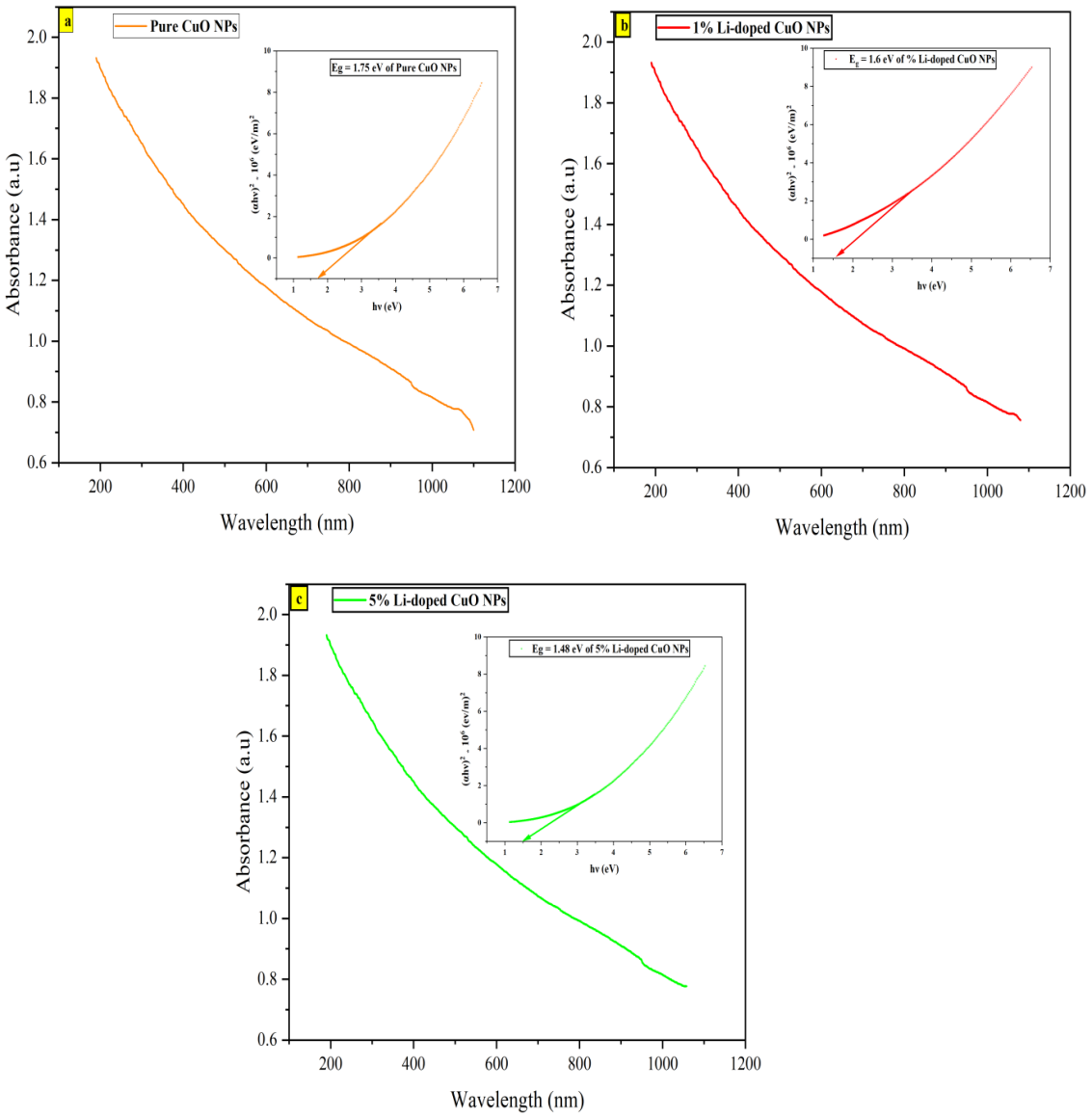


Fig. 4. Absorbance and Band gap spectra of (a) pure CuO NPs, (b)1% Li-doped CuO NPs, and (c)5% Li-doped CuO NPs, respectively.

CC BY

$$D=K\lambda/(\beta.\cos\theta) \quad (2)$$

where:

D is the crystallite size

K is a numerical factor frequently called the crystallite-shape factor = 0.9

λ is the wavelength of the X-rays (λ = 1.5406 Å).

β is the width (full-width at half-maximum) of the X-ray diffraction peak in radians.

θ is the Bragg angle.

Morphological Studies

The temperature, pH value, time and concentration of the initial species are important factors that affect nucleation and growth [57, 58] Careful tuning of these parameters enables control over the resultant physical and chemical properties of nanostructures. FESEM was used to analyze the ability of synthesized pure and Li-doped CuO NPs both for surface structure and particle size, as shown in Fig. 3.

As noted in all the FESEM images of (Figs. 3a–c), the spherical shape obtained was observed for all samples, but significant agglomeration has occurred. This agglomeration, which is a common phenomenon in metal oxide nanoparticles mainly

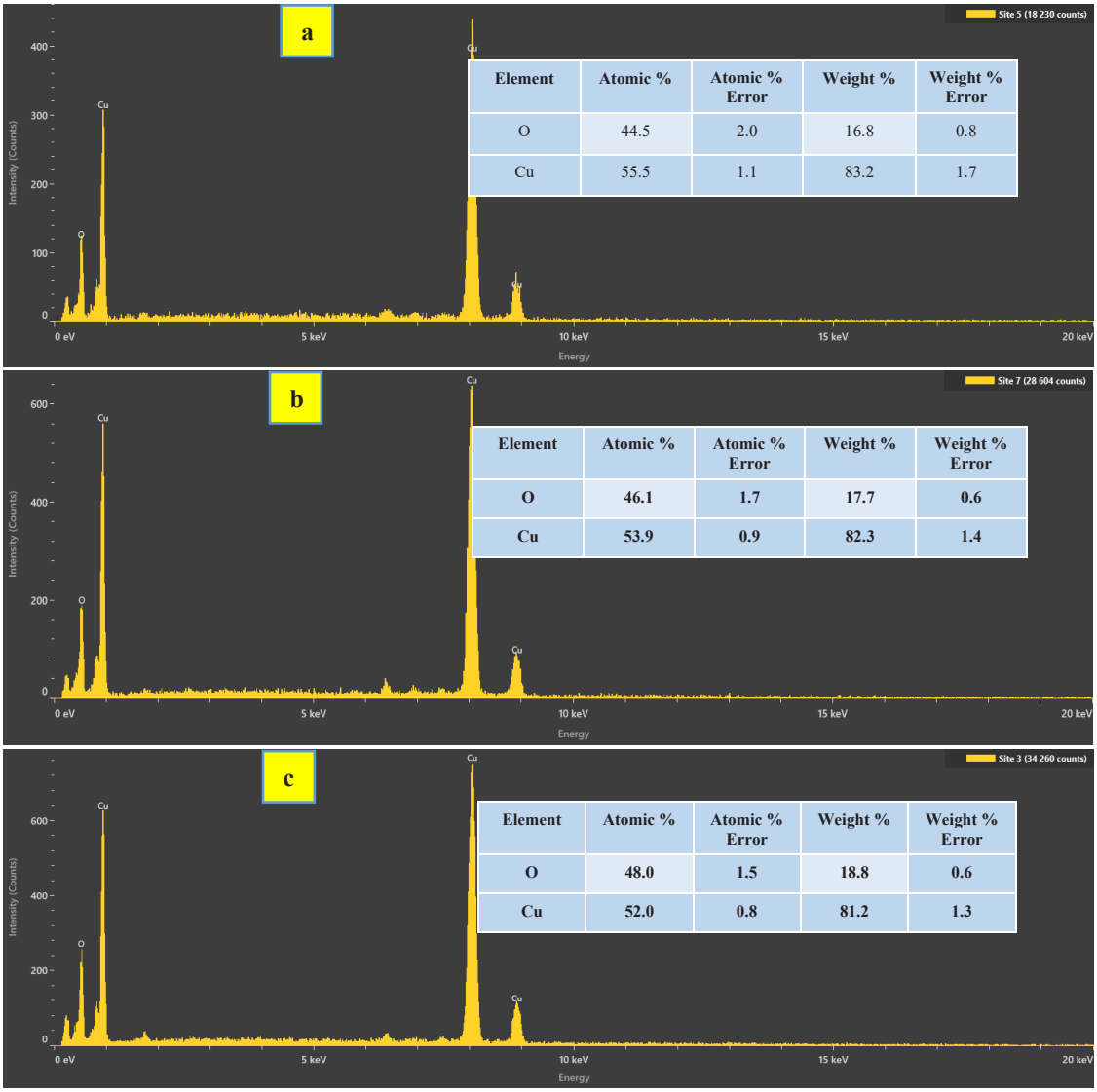


Fig. 5. EDS spectra of the sample (a) pure CuO, (b) 1% Li-doped CuO, and (c) 5% Li-doped CuO.

CC BY

originates from their large surface energy and strong interaction among the particles during preparation and heating.

For the pure sample, the particle size is around 48–68 nm. It is very easy to see that, when you add Li, the particles have a different size and distribution. For the 1% Li-doped sample, relatively small particles were observed with the size ranging from 39 to 65 nm. This is a consequence of the incorporation of Li^+ ions into the CuO lattice, which bends the lattice and may hinder crystal growth at its early stage of formation [59, 60].

On the other hand, when raising lithium up to 5%, a bigger particle size in the range of around 56-81 nm and a more noticeable agglomeration occur. These results indicate that elevated dopant concentrations increase interactions between particulates, and therefore facilitate aggregate formation and growth during the calcination process.

FESEM results indicated that the morphology and particle-size distribution of CuO NPs was significantly influenced by lithium doping. Smaller, less-doped particles might provide increased surface area, but more heavily doped systems would typically aggregate at high doping levels, lowering the active surface.

Instead, the increased antibacterial activity at higher concentration of lithium suggests that morphology is not the only explanation for material performance. This implies that the electronic structure and defect states are significantly altered whatever might be its x value which in turn is more important for getting functional properties required from Li-doped CuO NPs.

UV-visible Spectroscopy

Fig. 4 presents the optical properties of the synthesized samples, pure CuO NPs and doped CuO NPs, as determined from UV-visible absorption spectra measured in the wavelength range of 190-1200 nm. The optical band gap energy was determined using the Tauc relation formula Eq. 3:

$$\alpha=A\,(h\nu-E_g)^{1/2}/h\nu \quad (3)$$

where α, E_g, and A stand for the band gap, constant, and absorption coefficient, respectively [61, 62]. The optical band gap energy of pure CuO NPs was 1.75 eV, which decreases to 1.6 eV and 1.48 eV for 1% Li-doped and 5% Li-doped CuO NPs, respectively. These values are consistent with the previously reported values in the range of 1.2–1.9 eV for CuO nanostructures [63, 64].

The band gap decreases with the increase of Li concentration, which is attributed to the impurity levels and defects in the electronic structure. This phenomenon causes a band tailing and generates localized energy levels near the valence and conduction bands that are responsible for the renormalization of the band gap. Generally, CuO is a p-type, narrow-band gap semiconductor with mainly indirect electronic transitions [65–67].

Li+ ions alter the electronic structure and increase the defect concentrations that govern electronic transitions. The reduced band gap is important for the material's activity. A reduced band gap facilitates the excitation of electrons from the valence band to the conduction band, thus increasing the charge-carrier generation. The combined charge-carrier behavior enhances the surface redox reactions and facilitates the electron transfer.

This generation of ROS, including hydroxyl radicals (•OH) and superoxide anions (O_2^{-}•), is thus remarkably amplified. These ROS induce oxidative stress in bacterial cells, causing membrane damage that kills the cell. Thus, the enhanced antibacterial

Table 2. Quantities and diameters of the inhibitory zones for each bacterial species used.

Type of Bacteria	Concentration (µg/mL)	Inhibitory Zone Diameter (mm)		
		Pure CuO	1% Li-doped CuO	5% Li-doped CuO
E. faecalis	1024	21	23	26
	512	19	22	23
	256	16	20	21
	128	15	17	19
P. intermedia	1024	18	21	24
	512	16	18	22
	256	14	17	18
	128	13	13	15

CC BY

activity of CuO NPs is directly governed by Li-doping-induced optical modification.

Energy dispersive X-ray spectroscopy (EDS).

The elemental composition of pure and Li-doped CuO NPs obtained by the sol-gel method was examined by EDS analysis as shown in Fig. 5. The spectra of pure CuO and Li-doped CuO samples with 1 and 5% Li content showed the characteristic peaks of Cu and O confirming the formation of CuO as the main phase.

The intensity of the Cu-related peaks was

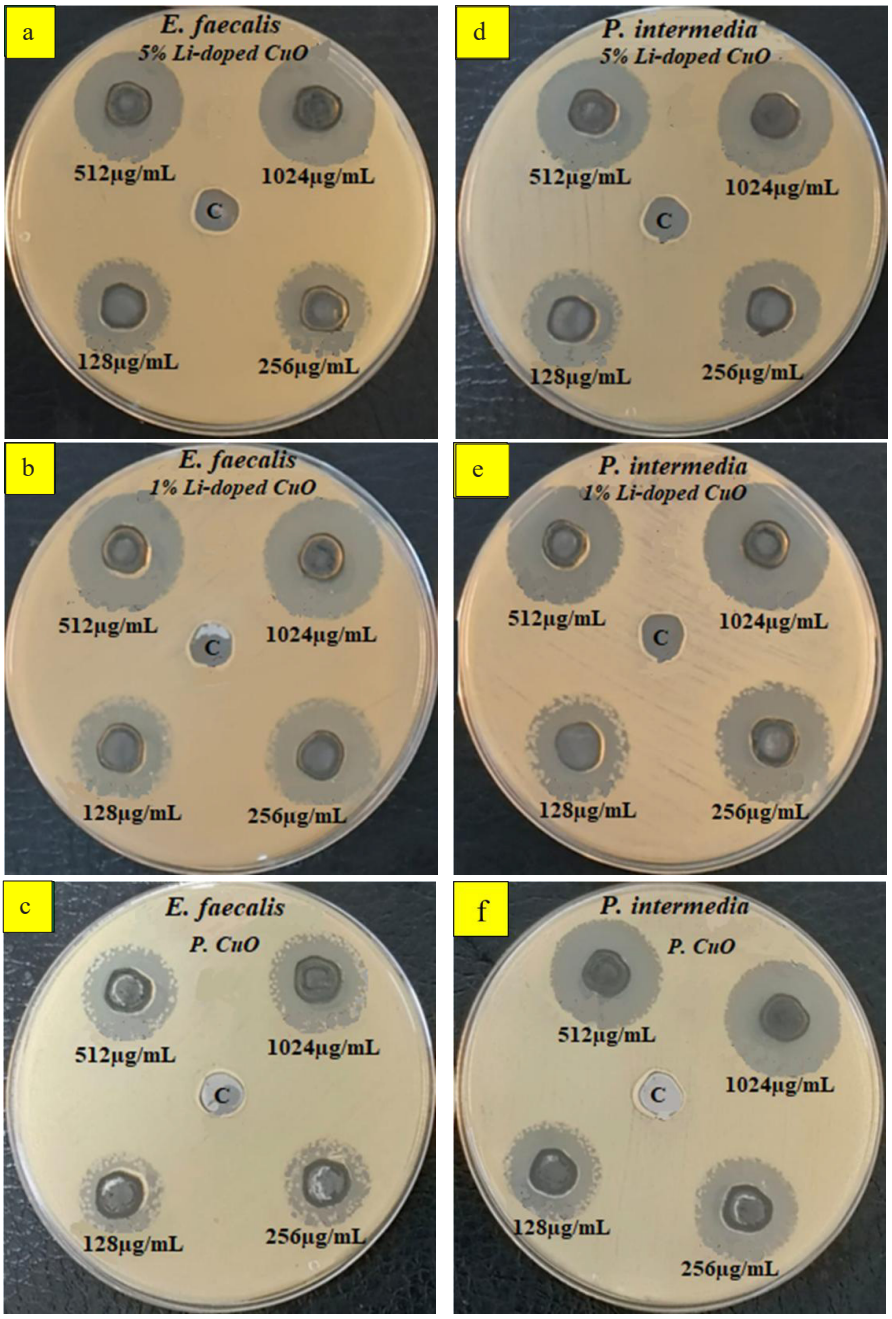


Fig. 6. Zones of inhibition of *E. faecalis*: (a) 5% Li-doped CuO NPs, (b) 1% Li-doped CuO NPs, and (c) pure CuO NPs; and of *P. intermedia* (d) 5% Li-doped CuO NPs, (e) 1% Li-doped CuO NPs, and (f) pure CuO NPs.

CC BY

higher in the Li-doped samples when compared with pure CuO, especially at higher Li content. This behavior was associated with the incorporation of Li ions into the CuO matrix and their interaction with Cu-related lattice sites. No apparent Li peak was observed which is expected due to the low atomic number of lithium and the low sensitivity of the conventional EDS for the light elements [68]. Further, the absence of additional impurity-related peaks indicates that Li doping did not induce any detectable secondary phases within the EDS detection limit.

Antibacterial Activity

The antibacterial activities of synthesized pure and Li-doped CuO NPs were evaluated against the Gram-positive *E. faecalis* and the Gram-negative *P. intermedia*. The results indicated that both the pure and doped samples were inhibitory; additionally, Li-doped CuO NPs exhibited much better antibacterial activity higher than that the pure samples. Overall, pure and doped samples showed higher activity against *E. faecalis* than *P. intermedia*. These differences were explained by structural differences in the bacterial cell wall and by their susceptibility to nanoparticles. The differences between Gram-positive and Gram-negative bacteria are based on the structure of the cell wall, peptidoglycan, and the absence of an outer membrane in Gram-positive bacteria, whereas Gram-negative bacteria have a relatively thin layer of peptidoglycan between an inner and an outer membrane. Consequently, Gram-positive bacteria are usually more susceptible to membrane disruption [69, 70]. In Table 2, the quantities and diameters of the inhibitory zones for each bacterial species used for the research are presented.

The antibacterial properties of pure and Li-doped CuO NPs were evaluated using the agar well diffusion method, as shown in Fig. 6. Each Petri dish had four wells, each containing a concentration of 128, 256, 512, or 1024 µg/mL.

Results clearly show concentration-dependent activity, with 5% Li-doped CuO NPs showing the largest inhibition zones against both *E. faecalis* and *P. intermedia,* Figs. 6a and d, followed by the 1% doped sample, Figs. 6b and e, while pure CuO NPs exhibit minimal activity, Figs. 6c and f.

None of the surface area or the morphological features described above accounts for this increased downhill antibacterial efficiency. The robustness of the enhanced antibacterial activity could be representative of the dominance of a different mechanism, as higher Li content is accompanied by larger crystallite sizes, which would otherwise reduce surface reactivity.

The most prominent reason attributed to this enhancement is Li-doping-induced defect engineering. The substitution of Cu^{2+} with Li^{+} induces charge imbalance within the CuO lattice, leading to the generation of oxygen vacancies and defect states. These defects act as charge-trapping sites, which help in the promotion of electron–hole separation and the generation of ROS such as •OH and O_2^{-}•. The generation of ROS is enhanced by oxidative stress, which causes significant damage to cellular frameworks and also causes cell death. The reduced band gap in Li-doped samples also facilitates electron excitation and surface redox reactions, thereby promoting ROS generation.

The antibacterial activity of Li-doped CuO NPs is mainly due to changes in their electronic structure. ROS are particularly noticeable when there are defects, rather than changes in the particle's size or shape. ROS attacks the bacterial membrane causing lipid peroxidation and increased membrane permeability. As a sequence, cell membrane interference permits leakage of intracellular components

such as proteins, ions, and nucleic acids. According to this steps, CuO/Li-doped CuO surface interface with bacterial cells may disturb membrane integrity through electrostatic interaction. Thus, Cu^{2+} ions are released and may contribute to toxicity by binding to proteins/enzymes and disturbing metabolic pathway.

CONCLUSION

The pure and Li doped CuO NPs were synthesized by using the sol-gel method. The average size of pure CuO NPs, 1% and 5% Li doped CuO were 28.6 nm, 34.5 nm, and 37.0 nm, respectively. The samples were also characterized by FESEM, XRD, and UV-vis spectroscopy. The surface morphology studies showed that the size distributions of pure and doped CuO NPs were 48 - 68 nm, 39 - 65 nm, and 56 - 81 nm, respectively. Furthermore, the XRD analysis confirmed the monoclinic structure of the nanoparticle samples.

Pure CuO NPs had lower antibacterial activity than doped CuO NPs. From the UV-visible absorption spectra, it was also observed that the energy gap of pure CuO was 1.75 eV, which is

CC BY

found to be higher than the previously reported value of 1% Li-doped CuO, 1.6 eV, and 5% Li-doped CuO, 1.48 eV.

The decreased energy gap of doped NPs suggests a better control over the synthesis, leading to enhanced optical properties. Li-doped CuO Nps exhibit a significantly better antibacterial activity at every concentration than pure CuO, which is attributed to defect engineering due to the Li incorporation. Hence, it causes a substantial improvement in the antibacterial properties even when the crystallite size is increased. This seemingly paradoxical observation can be explained by the introduction of oxygen vacancies and defect states within the lattice of CuO. This happens when Li^{+} ions replace or displace Cu^{2+} ions. These vacancies act as charge traps and help to decrease electron-hole recombination.

As a result, this process effectively charges separation. This process then leads to a significant increase in ROS levels, including superoxide anions and hydroxyl radicals.

The enhanced generation of ROS predominates over the negative effect of the reduced specific surface area associated with larger crystallite dimensions, resulting in greater damage to bacterial cells. Thus, electrical modifications caused by defects are the main factors affecting the antibacterial activity rather than morphological parameters. ROS attacks the bacterial wall causing permeable membrane. Leakage happens and ions are released and may contribute to toxicity by binding to proteins/enzymes and disturbing metabolic pathways.

For a more detailed investigation, more characterization parameters such as X-ray density, specific surface area, displacement density, stacking-fault probability and lattice strain can be measured. The extracted data will provide an insight into the physical and structural properties of the nanoparticles, thus verifying their functionality and potential applications.

CONFLICT OF INTEREST

The authors declare that there is no conflict of interests regarding the publication of this manuscript.

REFERENCES

1. Cao Y, Wong RCW, Jansisyanont P, Hariri F, Amir LR, Segarra MS, et al. Burden and Trends of Common Oral Disorders Across the Association of Southeast Asian Nations From 1990 to 2021. Int Dent J. 2026;76(2):109395.
2. Nwabunka M, Sowunmi AO, Osadolor UE, Akinyosoye AD, Nnyanzi L, Adeloye D, et al. Oral health in Africa: a neglected public health priority. Frontiers in Oral Health. 2026;7.
3. Lu W, Du W, Duan X. Global, Regional, and National Burden of Oral Diseases in Older Adults Aged 65 Years And Over. Int Dent J. 2026;76(1):109297.
4. Acharya S, Mathur MR, Tadakamadla SK, Brand A. Linking Health Financing to Oral Health Coverage and Disease Burden in SEARO Countries: A Cross-Sectional Analysis of Country Level Data. The International Journal of Health Planning and Management. 2025;41(1):47-58.
5. Wong G, Cheng K, Kumar T, Saponja M, Wright K, Ng A, et al. Dental Caries Risk and Prevention in Children and Adolescents With Special Needs: A Retrospective Cross-Sectional Study. Int J Paediatr Dent. 2025;36(1):195-206.
6. Molina A, Meyle J, Ram D, Chun YHP, Colmenares ME, Davidovich E. Periodontal Diseases and Conditions in Children and Adolescents Associated With Systemic Disorders: A Systematic Review. J Clin Periodontol. 2026;53(7):1199-1225.
7. Atanasov N, Borisov D, Evstatieva Y, Nikolova D. Effects of Probiotic Lactic Acid Bacteria on Oral Pathobionts and on Oral Health: A Review. Appl Microbiol. 2026;6(3):37.
8. Xiang Z, Liu Y. The pediatric oral mycobiome: a comprehensive review of its role in health and disease. Frontiers in Cellular and Infection Microbiology. 2026;16.
9. SheibaniNia A, Ghasemi Pirbalouti A, Rajabzadeh F, Hasanbarani M. Therapeutic potential of plant-based essential oils for dental disorders: A comprehensive review. Food Sci Biotechnol. 2026.
10. Shivakumar VH, Tegginamani AS, Shetty RM, Venkiteswaran A, Mohamad Zain N, Sarmin NIM, et al. Antimicrobial mechanism of Phyllanthus niruri L. against oral pathogens: a scanning and transmission electron microscopy study. Frontiers in Dental Medicine. 2026;7.
11. Reza N, Qader OAJA, Al-Rawas M, Omar M, Abdullah JY, Urmi SY. Enzyme-Based Mouthwashes for Oral Wound Healing and Xerostomia. European Journal of Dentistry. 2026.
12. Romandini M, Hajishengallis G, Curtis M, Baima G. Periodontal Medicine Rewired: Mechanisms Linking Periodontitis to Systemic Diseases. J Periodontal Res. 2026.
13. Gu Z, Chen X, Yin C, Zhou Y, Song L, Wu K, et al. Antimicrobial peptides for bacterial infections and their biomedical applications. Discover Nano. 2026;21(1).
14. Maan M, Joshi S, Barman P, Sharma S, Saini A. Development of a synthetic antimicrobial peptide targeting MDR wound pathogens and biofilms: effective therapeutics for chronic wound management. Journal of Materials Chemistry B. 2026;14(22):6862-6889.
15. Liu T, Qin M, Lu Y, Sun W, Fu X, Huang S, et al. Heterojunction with Photo-Responsive Therapy against Multidrug-Resistant Bacteria for Rapid Sterilization and Improved Burned Wound Healing. Advanced Healthcare Materials. 2025;15(11).
16. Elshobary ME, Badawy NK, Ashraf Y, Zatioun AA, Masriya HH, Ammar MM, et al. Combating Antibiotic Resistance: Mechanisms, Multidrug-Resistant Pathogens, and Novel Therapeutic Approaches: An Updated Review. Pharmaceuticals. 2025;18(3):402.
17. Sim HT, Gençaslan M, Merdan M. Synthesis of MgO Nanoparticles via the Sol–Gel Method: A DFT+U Analysis and Antibacterial Efficacy Comparison with Commercial

CC BY

Counterparts. Journal of Superconductivity and Novel Magnetism. 2025;38(3).
18. Rakshit S, Roy T, Samanta A, Datta R, Jana PC, Gupta K. Multifunctional Biogenic Copper Oxide Nanoparticles: A Comprehensive Review on Biomedical Applications, Photocatalytic Wastewater Treatment, and Future Perspective. ChemistrySelect. 2025;10(43).
19. Saleem MH, Ejaz U, Vithanage M, Bolan N, Siddique KHM. Synthesis, characterization, and advanced sustainable applications of copper oxide nanoparticles: a review. Clean Technologies and Environmental Policy. 2024;27(10):5719-5744.
20. Obaid AN, Abdelghany TM, Soliman AM, Mahmoud NN, Mekky AE. Green mycosynthesis of a CuO/ZnO heterojunction nanocomposite using Aspergillus terreus and its antibacterial and anti-virulence activity against multidrug-resistant Escherichia coli. Sci Rep. 2026;16(1).
21. Gupta N, Singh R, Loveleen L, Bunkar T, Nimesh S. Breaking the Biofilm Fortress: Copper and Copper Oxide Nanoparticles as Next-Gen Antimicrobials. ChemistrySelect. 2026;11(21).
22. Huang Y, Wan X, Su Q, Zhao C, Cao J, Yue Y, et al. Ultrasound-activated piezo-hot carriers trigger tandem catalysis coordinating cuproptosis-like bacterial death against implant infections. Nature Communications. 2024;15(1).
23. Zhang Z, Xue H, Xiong Y, Geng Y, Panayi AC, Knoedler S, et al. Copper incorporated biomaterial-based technologies for multifunctional wound repair. Theranostics. 2024;14(2):547-570.
24. Lopez ECR. Polymeric Composite Beads for Pollutant Removal in Water. ChemistrySelect. 2026;11(4).
25. Khan A, Kumar T, Muthukrishnan M, Thiagamani SMK, Alzahrani KA, Ayyar M, et al. Correction to: Investigating the role of rare earth ion as dopant and Co-dopant in Cuo NPs for high frequency applications. Journal of Materials Science: Materials in Electronics. 2026;37(18).
26. Tatar DK, Jaiswal Y, Pal SL. Carbon nanofiber-encapsulated CuO nanoparticles: High-performance anode material for lithium-ion batteries. Mater Lett. 2025;397:138841.
27. Yuan J, Gu X, Zhilin X, Zhang X, Cao J, Chen H, et al. Microbial of low-concentration antisite defects LiFePO4 for boosting lithium ion capture. Nano Today. 2025;64:102781.
28. Liu S, Tang Y, Zhang X, Zhang Y. Lithium-doped mesoporous bioactive glass with dual antibacterial mechanisms: Sustained ion release and osteogenic activity for bone regeneration. Colloids Surf Physicochem Eng Aspects. 2025;727:138356.
29. Chen Y, Liu F, Chen H, Huang Y, Li Y, Jin Q, et al. Self-assembled copper-phenolic nanoparticles for antimicrobial therapy by triggering Fenton reaction and cuproptosis-like bacterial death. Nano Today. 2025;65:102850.
30. Su S, Wei S, Zhou Y, Wang Y, Wang Y. A carrier-free hydrogel deriving from bioactive herbal polysaccharide and Cu^{2+} for healing MRSA-infected diabetic wound by coupling with self-regulated cascade enzyme-mimicking catalytic and photothermal therapy. Chem Eng J. 2026;533:174546.
31. Abood ES, Sim HT. Magnesium Oxide NPs Carbon Paste Ion-Selective Electrode Industrialization and Potentiostat Cyclic Voltammetry Detections for Determination of Mg+Ion in Various Solutions. Annales de Chimie - Science des MatériauxA. 2025;49(2):213-218.
32. Sim HT, Gençaslan M, Merdan M. Synthesis of MgO nanoparticles via the sol-gel method for antibacterial applications, investigation of optical properties and comparison with commercial MgO. Discover Applied Sciences. 2024;6(11).
33. Kumar AN, Balakrishna M, Desai U, Rakshith R, Ambika KM, Soumya P, et al. Solution combustion synthesis of ZnO doped CuO nanocomposite for photocatalytic and sensor applications. Sci Rep. 2025;15(1).
34. Hjiri M, Mustapha N. Sol–gel derived ZnO nanoparticles doped with transition and alkaline-earth metals: a comprehensive review on dielectric and electrical properties. J Sol-Gel Sci Technol. 2025;116(2):1167-1187.
35. Dhotre SB, Lonkar SP, Bhosale AS, Mali NP, Kaswan P, Mene RU, et al. Solar-driven degradation of eosin Y using Cu–TiO_2 Photocatalysts: A comparative study of sol–gel and hydrothermal synthesis routes. Inorg Chem Commun. 2026;184:115943.
36. Boujelbene W, Kharrat ABJ, Kammoun S, Chniba-Boudjada N, Khirouni K, Boujelben W. Investigation of structural and optical properties of SmCrO3 orthochromite compound prepared via sol–gel process. Ionics. 2025;31(3):3037-3052.
37. Zeng Y, Lu Q, Li C, Dou A, Zhou Y, Su M, et al. Synthesis of porous carbon $Na_4Fe_3(PO_4)_2P_2O_7$@C by sol-gel method as a high-rate cathode for sodium-ion batteries. Electrochimica Acta. 2025;520:145871.
38. Yang M, Wang S, Dong Z, Yang B, Qu T. Extracting metallic lithium and separating diffusion pump oil from lithium slag using a novel negative pressure distillation technology. Sep Purif Technol. 2025;362:131821.
39. Akbar HM, Habib S, Akoumeh R, Mahdi E, Al-Ejji M, Altaee A, et al. Lithium Extraction Methodology and Recovery from Conventional Resources: A Critical Review. Water, Air, and Soil Pollution. 2025;236(11).
40. Muaz, Bin Riaz S, Hassan M. Mechanochemical Approaches for Advancing Lithium-Ion Battery Materials: Synthesis, Processing, and Performance Enhancement. Mechanics Exploration and Material Innovation. 2025;2(1):49-58.
41. Ravishankar TN, Reddy RM, Adarsha JR, Harisha S, Ravishankar PN, Ananda A, et al. Role of Ionic Liquids in Hydrothermal Synthesis of Li-Doped CuO Nanoparticles: Improved Photocatalytic, Electrochemical, and Antibacterial Properties. ChemistrySelect. 2026;11(6).
42. Kiran Kumar MC, Santhosh Kumar MV, Kirthan BR, Nagaraja KK, Madhu S. Studies on, sustainable bio-fuel-assisted combustion synthesis of CuO/MgO nanocomposites for conductance and opto-electrocatalytic applications. Materials Chemistry and Physics. 2026;362:132736.
43. Azzoug A, Baka O, Laidoudi S, Boudour S, Belgherbi O, Tabti L, et al. Fabrication of CuO thin films via Cu_2O electrodeposition and subsequent annealing: a potential-dependent study. J Chin Chem Soc. 2025;73(2):386-398.
44. Bhattacharjee PR. Discovery of the lack of success of Bragg's law in respect of perfect quantification of the X-ray diffraction phenomenon. Next Research. 2025;2(2):100312.
45. Awad H, Hamdy KH, Yasser Y, Magdy S, Phlip N, Fawzy N, et al. Plasmonic and magnetic ZnO-based nanocomposites for enhanced photocatalysis and ultrasensitive SERS detection of malachite green. Sci Rep. 2026;16(1).
46. Xia X, Liu J, Zhu H, Meng Y, Tan S, Yuan C, et al. Research progress on NASICON-type solid electrolytes in all-solid-state sodium batteries: bulk optimization and interfacial regulation. RSC Advances. 2026;16(35):33630-33651.
47. Stalin M, Alqahtani T, Ravula SR, Charmakani J, Perumal T, V KA, et al. Anticancer and Larvicidal Evaluation of

CC BY

Methyl Ionone-loaded PEG-functionalized Copper Oxide Nanoparticles: In Silico Insights Into Insecticide Resistance. J Pharm Innov. 2026;21(4).
48. Athar T, Hakeem A, Ahmed W. Synthesis of MgO Nanopowder via Non Aqueous Sol–Gel Method. Advanced Science Letters. 2012;7(1):27-29.
49. Mashuni M, Zaeni A, Fadila D, Fitri N, Jahiding M, Milen Y. Esterification of Sago Dregs Bio-Oil Using Zeolite Modified MgO for Biofuel Applications. International Journal of Energy Production and Management. 2026;11(1):190-202.
50. Jawad HM, Rasheed RT, Kułacz K, Abdullah TA. Synthesis and characterization of MgO and Al_2O_3 nanoparticles for the adsorptive removal of methyl violet 6B dye from contaminated water. Inorg Chem Commun. 2026;191:116857.
51. Gopinathan N, Sathik Basha S, Mubeen M, Jayaprakash RN, Mariappan R, Melwin G, et al. Synthesis, structural and optical properties of $Cs_3Bi_2I_9$, $Rb_3Bi_2I_9$ and Ho3Bi2I9 perovskite-structured semiconductors for optoelectronic applications. Indian Journal of Physics. 2026;100(6):2307-2316.
52. Jiang Z, Lou Y, Fu Z, Ruan H, Long Y. Influence of particle size distribution on the microstructure, density and ionic conductivity of $Li_{6.25}Ga_{0.25}La_3Zr_2O_{12}$ ceramics. Ceram Int. 2025;51(23):38712-38722.
53. Han Y, Lei Y, Ni J, Zhang Y, Geng Z, Ming P, et al. Single-Crystalline Cathodes for Advanced Li-Ion Batteries: Progress and Challenges. Small. 2022;18(43).
54. Luthra P, Sharma B, Tomar M, Sharma A, Chowdhuri A, Gupta R. Hydrothermally synthesized Li-KNN and PVDF based flexible composites for piezoelectric energy harvesting. Materials Science and Engineering: B. 2026;332:119635.
55. Fernando WTRS, Amaraweera THNG, Jayathilaka KMDC, Kumara LSR, Seo O, Osaka K, et al. Engineering electron density and structural properties of CuO anode material via calcination and in situ synchrotron XRD for enhanced lithium-ion battery performance. Journal of Materials Science. 2025;60(48):25386-25408.
56. Deng Z, Ma Z, Li Y, Li Y, Chen L, Yang X, et al. Boosting Lithium-Ion Storage Capability in CuO Nanosheets via Synergistic Engineering of Defects and Pores. Frontiers in Chemistry. 2018;6.
57. Asgar Pour Z, Alassmy YA, Sebakhy KO. A Survey on Zeolite Synthesis and the Crystallization Process: Mechanism of Nucleation and Growth Steps. Crystals. 2023;13(6):959.
58. Zhang Y, Li B, Liu J, Han D, Rohani S, Gao Z, et al. Inhibition of Crystal Nucleation and Growth: A Review. Crystal Growth and Design. 2024;24(6):2645-2665.
59. Kaur G, Gates BD. Review—Surface Coatings for Cathodes in Lithium Ion Batteries: From Crystal Structures to Electrochemical Performance. J Electrochem Soc. 2022;169(4):043504.
60. Li S, Lee J-H, Hwang SM, Kim Y-J. Reversible flowering of CuO nanoclusters via conversion reaction for dual-ion Li metal batteries. Nano Convergence. 2023;10(1).
61. Kabasinskas E, Karoblis D, Griesiute D, Raudonyte-Svirbutaviciene E, Pazylbek S, Lemezis R, et al. Synthesis and morphological control of Ca5(PO4)3Cl and Ca_2PO_4Cl via the phase transformation of amorphous calcium phosphate in molten chlorides. Ceram Int. 2024;50(10):16844-16851.
62. Karazmoudeh NJ, Soltanieh M, Hasheminiasari M. Structural and photocatalytic properties of undoped and Zn-doped CuO thin films deposited by reactive magnetron sputtering. J Alloys Compd. 2023;947:169564.
63. Chewaka D, Abate D, Urga K. Growth Inhibition of Grain Spoilage Fungi by Selected Herbs and Spices Essential Oils. Science, Technology and Arts Research Journal. 2015;3(4):135.
64. Ahmed AM, Fadhil GA, Rahmah MI. Innovative use of commercial wipes as a template for the synthesis of ZnO and CuO nanoparticles via combustion method for antibacterial applications. Applied Nanoscience. 2026;16(1).
65. Yang L, Li W, Huang D, Guan J, Wei Z, Yuan T, et al. Bandgap Engineered λ-MnO_2 for Highly-Efficient Solar-Driven Lithium Selective Extraction and Freshwater Generation from Saline Lake Brine. Adv Funct Mater. 2025;36(9).
66. Zhou F, Gong Z, Wang R, Guo M, Zeng R, Li Y, et al. Band Structure and Spin-State-Induced Electronic Configuration Regulation for Efficient Sulfur Redox Reaction. Adv Funct Mater. 2024;35(12).
67. Meziane K, El Hichou A, El Hamidi A, Chhiba M, Bourial A, Almaggoussi A. Li concentration dependence of structural properties and optical band gap of Li-doped ZnO films. Appl Phys A. 2017;123(6).
68. Golla-Schindler U, Schneider G. EDS with Low-Voltage SEM: Possibilities and limitations of lithium detection and quantification. EPJ Web of Conferences. 2026;349:01004.
69. Wang Z, Ma J, Lin J, Li C, Xiang Y, Yu Z, et al. Antibacterial effects of BB-Cl-Amidine against multidrug-resistant Gram-positive pathogens via membrane disruption. The Journal of Antibiotics. 2025;79(1):30-40.
70. Xu F, Xie Y, Yu W, Wang Z. Breaking the outer membrane barrier: structure, targets, and antimicrobial strategies for Gram-negative bacteria. Front Microbiol. 2026;17.

CC BY